Very high cycle fatigue life and critical defect size: Modeling of statistical size effects

Received: 15 December 2020 | Revised: 12 January 2021 | Accepted: 17 January 2021

DOI: 10.1111/ffe.13424

ORIGINAL CONTRIBUTION

FFEMS Fatigue & Fracture of Engineering Materials & Structures WILEY

Very high cycle fatigue life and critical defect size: Modeling of statistical size effects

Davide S. Paolino

Department of Mechanical and Aerospace Engineering, Politecnico di Torino, Turin, Italy

Correspondence
Davide S. Paolino, C.so Duca degli Abruzzi 24, Department of Mechanical and Aerospace Engineering, Politecnico di Torino, 10129 Turin, Italy.
Email: davide.paolino@polito.it

Abstract

A novel statistical approach to model size effects in very high cycle fatigue (VHCF) is proposed in the paper. The statistical distributions of the VHCF life and of the size of the defect leading to VHCF failure (critical defect) are identified in the paper through the weakest-link principle. The statistical distributions are able to account for the stress gradients that are present in a loaded material volume. An efficient procedure for estimating the parameters involved in the statistical distributions is also shown. The proposed statistical models are finally validated through experimental data taken from the literature. The experimental validation proves the fitting capability of the proposed models that outperform the traditional models based on the 90% risk-volume.

KEYWORDS

risk-volume, stress gradients, uniformly stressed volumes, very high cycle fatigue, weakest-link principle

1 | INTRODUCTION

In many applications, machinery components subjected to fatigue loading must be designed in the so-called very high cycle fatigue (VHCF) region, to sustain even more than 10^8 cycles. Automotive components,[1–4] high-speed train components,[3–7] aircraft components,[3,4,8–12] as well as nuclear structural components[13] represent some examples of components to be designed in the VHCF region. The need to prevent the failure of these components is one of the main reasons for the growing interest toward the research on the VHCF response of materials.

Currently, the VHCF research focuses on the mechanisms behind the crack initiation and researchers generally agree about the experimental evidence that the VHCF crack originates from the weakest site within the most stressed volume, the so-called risk-volume (or control-volume, or highly stressed volume[14,15]). The weakest site in fatigue is generally represented by a defect (inclusion, pore, matrix inhomogeneity) that acts as an initial crack[16,17] in the loaded material volume. This is well known in the fatigue literature (see, e.g., the works on manufacturing defects in cast irons[18–24] and additive materials[25–30]). The defect population drives the VHCF response of materials, and according to Murakami,[17,31,32] the defect size is the main responsible for the VHCF failure. In particular, the largest defect in the risk-volume is generally assumed to nucleate the crack leading to the VHCF failure. Defects are randomly distributed within the risk-volume and, according to Murakami[17] and Beretta et al.,[33] the distribution of the defect size in materials is statistically dependent on the material volume: the larger the material volume, the larger the probability of large defects. Furthermore, the larger the defect, the smaller the VHCF strength, following Murakami's theory.[17,31,32] This is the rationale behind size effects in VHCF: larger loaded volumes may include larger defects that negatively affect the VHCF response.

Size effects in VHCF have been recently investigated in the literature.[14,25,26,34-45] In all cases, VHCF tests have been run with ultrasonic fatigue testing machines and size effects have been assessed by testing specimens with different risk-volumes, under tension–compression loading cycles. Experimental results reported in previous studies[26,34–36,38,39,44] have shown that size effects significantly affect the VHCF response and must be carefully considered when designing components against VHCF failure.

The computation of the risk-volume plays a major role when quantifying size effects in VHCF. It is generally acknowledged[17,24,25,34–48] that the risk-volume corresponds to the material volume with stresses larger than the 90% of the maximum stress in the whole loaded volume. This is generally referred to as 90% risk-volume. The reason for this definition is that defects leading to failure (critical defects) are most likely located in the region where the applied stress is larger than a sufficiently large threshold. However, the choice for the threshold value could be not uniquely defined, depending on the investigated material. Generally, 90% risk-volume have been considered in the literature.[17,24,25,34–48] However, a 95% risk-volume has been used in Fitzka et al.,[49] and in Furuya,[34] VHCF failures have been found for defects outside the 90% risk-volume, in particular for applied stresses equal to 83% and 88% of the maximum stress. In the latter case, the 90% risk-volume provides a smaller, thus nonconservative, estimate of the volume to be considered for quantifying size effects.

Furthermore, according to the statistics of extremes[17,33,50] a change in the considered threshold implies, for the same critical defect sizes, a change in the parameters involved in the statistical distribution of the critical defect size, which is not physically admissible: parameter estimates should only depend on the investigated material and not on the threshold considered for computing the risk-volume. Therefore, the risk-volume concept may lead to an inaccurate assessment of size effects in VHCF, and it is in need of a revision for preventing nonconservative design of machinery components against VHCF failure.

In the present paper, the concept of risk-volume is revised in a statistical framework. Novel statistical models, based on the weakest link principle, are provided, with the aim of accounting for size effects with no need of defining a risk-volume. The proposed statistical models can consider stress gradients within the loaded volume and involve actual material parameters that only change if the material changes. The proposed statistical models are finally validated through several experimental datasets taken from the literature and from VHCF tests run by the author and his coworkers.

2 | CRITICAL DEFECT SIZE AND CONDITIONAL VHCF LIFE: PRELIMINARY DEFINITIONS

In a loaded volume, the defect that originates the fatigue failure is referred to as critical defect. To identify the critical defect in a loaded volume, both the defect size and the local stress in the proximity of the defect must be considered. Indeed, large defects in a lightly stressed region may be less critical than small defects in a highly stressed region, following the stress intensity factor definition.

Figure 1 shows the variation of the uniformly stressed volumes with the local stresses, in a Gaussian specimen[37] subjected to an ultrasonic VHCF test. The stress distribution within the specimen, which is depicted in Figure 1, can be obtained with a finite element model (FEM) of the tested specimen.

Two different large volumes with constant stress are highlighted in Figure 1: the first one, v_i, is in a region with stress equal to 13.75% of the maximum stress; the second one, v_j, is larger and in a region with larger stress (equal to 92.75% of the maximum stress). Volume v_j is the one subjected to a larger stress and, according to the statistics of extremes,[17,33,51] is the one with larger probability of including a large defect. Therefore, if compared to v_i, v_j more probably contains the critical defect. However, if smaller volumes with larger stress are considered, the evaluation becomes more difficult, and it can be only quantified by defining the statistical distribution of the criticality associated to each volume.

In each uniformly stressed volume, the largest defect is the most critical one, and it can be identified with the square-root of area approach suggested by Murakami[17] and Beretta et al.[33] It is well known[17,33,50,52] that the largest defect, denoted as $\sqrt{A}$, follows a truncated largest extreme value distribution (LEVD) with parameters $\mu_{\sqrt{A}}$ and $\sigma_{\sqrt{A}}$ and defined for positive defect sizes. Equation 1

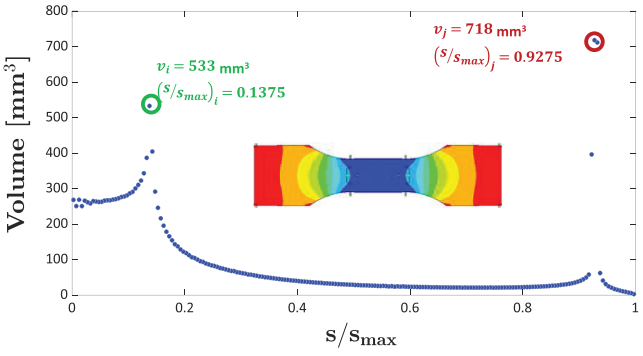

FIGURE 1 Distribution of uniformly stressed volumes in a Gaussian specimen subjected to an ultrasonic very high cycle fatigue (VHCF) test (stress field in the specimen is also depicted) [Colour figure can be viewed at wileyonlinelibrary.com]

reports the probability density function (pdf) for the largest defect contained in volume v_i:

$$f_{\sqrt{A_i}}(\sqrt{a};v_i)=\frac{1}{\sigma_{\sqrt{A}}}\frac{\varphi_L\left(z_{\sqrt{A_i}}(\sqrt{a})\right)}{1-\phi_L\left(z_{\sqrt{A_i}}(0)\right)}, \tag{1}$$

where $\varphi_L\left(z_{\sqrt{A_i}}(\sqrt{a})\right)=e^{-z_{\sqrt{A_i}}(\sqrt{a})-e^{-z_{\sqrt{A_i}}(\sqrt{a})}}$ is the pdf of the standardized LEVD, evaluated at $z_{\sqrt{A_i}}(\sqrt{a})=\frac{\sqrt{a}-\left(\mu_{\sqrt{A}}+\sigma_{\sqrt{A}}\log(v_i)\right)}{\sigma_{\sqrt{A}}}$, and $\phi_L\left(z_{\sqrt{A_i}}(0)\right)=e^{-e^{-z_{\sqrt{A_i}}(0)}}$ is the cumulative distribution function (cdf) of the standardized LEVD, evaluated at $z_{\sqrt{A_i}}(0)=-\frac{\mu_{\sqrt{A}}+\sigma_{\sqrt{A}}\log(v_i)}{\sigma_{\sqrt{A}}}$.

Each uniformly stressed volume is characterized by a specific stress level and by a specific distribution for the largest defect size. If volume v_i is considered, then a given largest defect size $\sqrt{a_i}$, which is randomly extracted from $f_{\sqrt{A_i}}(\sqrt{a})$, and a given local stress level s_i must be taken into account to estimate the VHCF life associated to v_i. Indeed, it is well known in the literature[16,17,32,51,52] that the VHCF life depends both on the stress amplitude and on the defect size. It is worth to note that, to simplify the statistical model, several approximations must be tolerated (e.g., defect shape and composition as well as three-dimensional effects[53,54] at the initial defect are not taken into account). However, provided that the estimated statistical model well fits the experimental data, then all the approximations involved in the model can be considered as cancelled out in the fitting phase.

According to previous works,[51,55–57] the VHCF life (i.e., the logarithm of the number of cycles to failure) follows a normal distribution with constant standard deviation σ_Y and mean value that linearly depends on the logarithm of the stress amplitude (Basquin's model) and on the logarithm of the largest defect size (square-root of area model proposed by Murakami[17] and stress intensity factor relevance[58,59]). In particular, the cdf of the VHCF life for a given largest defect size $\sqrt{a_i}$ and applied stress s_i is given by

$$F_{Y_i|\sqrt{a}}(y;s_i,\sqrt{a_i})=\phi_G\left(\frac{y-\mu_{Y,i}(s_i,\sqrt{a_i})}{\sigma_Y}\right), \tag{2}$$

where $Y_i|\sqrt{a}$ denotes the conditional random variable (rv) VHCF life given the defect size, $\phi_G(\cdot)$ is the cdf of standardized Normal distribution, and the mean value $\mu_{Y,i}$ is as follows:

$$\mu_{Y,i}(s_i,\sqrt{a_i})=c_Y+m_Y\log_{10}\left(s_{max}\left(\frac{s_i}{s_{max}}\right)\right)+n_Y\log_{10}(\sqrt{a_i}), \tag{3}$$

where c_Y, m_Y, and n_Y are constant parameters and s_{max} is the maximum stress in the whole volume.

3 | STATISTICAL DISTRIBUTION OF THE (MARGINAL) VHCF LIFE

According to the definition of marginal cdf,[51,52] the expression of the marginal cdf for the VHCF life related to volume v_i is given by

$$F_{Y_i}(y;s_i,v_i)=\int_0^{\infty}\phi_G\left(\frac{y-\mu_{Y,i}(s_i,\sqrt{a})}{\sigma_Y}\right)f_{\sqrt{A_i}}(\sqrt{a},v_i)d\sqrt{a}, \tag{4}$$

where $f_{\sqrt{A_i}}(\sqrt{a},v_i)$ is reported in Equation 1.

The marginal cdf in Equation 4 is related to volume v_i. Similar expressions can be obtained for the other uniformly stressed volumes $v_1,v_2,...,v_{n_s}$, being n_s the total number of uniformly stressed volumes.

According to the weakest-link principle,[14] the smallest VHCF life among the VHCF lives related to all the uniformly stressed volumes represents the VHCF life of the whole loaded volume. The cdf of the smallest VHCF life can be computed from the product of the reliabilities related to each volume:

$$F_Y(y;(s_1,v_1),...(s_{n_s},v_{n_s}))=1-\prod_{i=1}^{n_s}R_{Y_i}(y;s_i,v_i), \tag{5}$$

where $R_{Y_i}(y;s_i,v_i)=1-F_{Y_i}(y;s_i,v_i)$ is the reliability related to volume v_i and $F_{Y_i}(y;s_i,v_i)$ is the marginal cdf in Equation 4. Equation 5 shows that the cdf of the (marginal) VHCF life for the whole loaded volume depends on all the couples (s_i,v_i), being $i=1,...,n_s$.

4 | STATISTICAL DISTRIBUTION OF THE CRITICAL DEFECT SIZE

The infinitesimal probability of having, in volume v_i, a largest defect size smaller than $\sqrt{a}$ and a VHCF life in the range $(y; y+dy]$ is given by

$$f_{Y_i,\sqrt{A_i}\le\sqrt{a}}(y,\sqrt{a};s_i,v_i)=\int_0^{\sqrt{a}}\frac{1}{\sigma_Y}\varphi_G\left(\frac{y-\mu_{Y,i}(s_i,\sqrt{a})}{\sigma_Y}\right)f_{\sqrt{A_i}}(\sqrt{a},v_i)d\sqrt{a}, \tag{6}$$

where $f_{Y_i,\sqrt{A_i}\le\sqrt{a}}(y,\sqrt{a};s_i,v_i)dy = P[(y<Y_i|\sqrt{a}\le y+dy)\cap(\sqrt{A_i}\le\sqrt{a})]$, $\varphi_G(\cdot)$ is the pdf of the standardized Normal distribution, and $f_{\sqrt{A_i}}(\sqrt{a},v_i)$ is reported in Equation 1.

If all the other uniformly stressed volumes have marginal VHCF life larger than y, then v_i becomes the critical uniformly stressed volume, that is, the uniformly stressed volume that contains the critical defect, and $\sqrt{A_i}$ becomes the critical defect size, $\sqrt{A_c}$:

$$P\left[\left(y<Y_i|\sqrt{a}\le y+dy\right)\cap\left(\sqrt{A_c}\le\sqrt{a}\right)\cap(v_i\text{ is critical})\right] = f_{Y_i,\sqrt{A_i}\le\sqrt{a}}(y,\sqrt{a};s_i,v_i)\prod_{\substack{j=1\\ j\neq i}}^{n_s} R_{Y_j}(y;s_j,v_j). \tag{7}$$

To define the cdf of the critical defect size is necessary to integrate over the range of variation of the VHCF life and to sum up the probabilities related to each uniformly distributed volume:

$$F_{\sqrt{A_c}}\left(\sqrt{a};(s_1,v_1),\ldots(s_{n_s},v_{n_s})\right) = \sum_{i=1}^{n_s}\int_{-\infty}^{+\infty} f_{Y_i,\sqrt{A_i}\le\sqrt{a}}(y,\sqrt{a};s_i,v_i)\prod_{\substack{j=1\\ j\neq i}}^{n_s} R_{Y_j}(y;s_j,v_j)dy. \tag{8}$$

Equation 8 shows that the cdf of the critical defect size depends on all the couples (s_i, v_i), being $i = 1,\ldots,n_s$.

5 | STATISTICAL DISTRIBUTION OF THE CRITICAL VOLUME

The critical volume is, in the whole volume, the uniformly stressed volume that contains the critical defect. The probability that the ith uniformly stressed volume is critical corresponds to the probability that the VHCF life related to v_i, Y_i, is the minimum VHCF life in the whole loaded volume:

$$P[v_i\text{ is critical}] = P[Y_{min}=Y_i] = P\left[(y<Y_i\le y+dy)\bigcap_{\substack{j=1\\ j\neq j}}^{n_s} Y_j>y, \forall y\in\mathbb{R}\right]. \tag{9}$$

The infinitesimal probability of having $y < Y_i \le y + dy$ is related to the pdf of Y_i, which can be easily obtained from Equation 4:

$$f_{Y_i}(y;s_i,v_i) = \frac{\partial F_{Y_i}(y;s_i,v_i)}{\partial y} = \int_0^{\infty}\varphi_G\left(\frac{y-\mu_{Y,i}(s_i,\sqrt{a})}{\sigma_Y}\right)f_{\sqrt{A_i}}(\sqrt{a},v_i)d\sqrt{a}. \tag{10}$$

The reliability $R_{Y_j}(y;s_j,v_j)$ corresponds to the probability of having $Y_j > y$. Therefore, the probability that v_i is critical is the integral, over the domain of the VHCF life, of the product of $f_{Y_i}(y;s_i,v_i)$ times all the reliabilities $R_{Y_j}(y;s_j,v_j)$, being $j = 1,\ldots,i-1,i+1,\ldots,n_s$:

$$p_{V_c}(v_i) = P[V_c=v_i] = \int_{-\infty}^{+\infty} f_{Y_i}(y;s_i,v_i)\prod_{\substack{j=1\\ j\neq i}}^{n_s} R_{Y_j}(y;s_j,v_j)dy, \tag{11}$$

where V_c denotes the critical volume rv. Equation 11 is the probability mass function of the discrete rv V_c. The cdf of V_c is thus equal to

$$F_{V_c}(v_i) = P[V_c\le v_i] = \sum_{j=1}^{i}\int_{-\infty}^{+\infty} f_{Y_j}(y;s_j,v_j)\prod_{\substack{k=1\\ k\neq j}}^{n_s} R_{Y_j}(y;s_k,v_k)dy, \tag{12}$$

where $i = 1,\ldots,n_s$. Equation 12 can be used to quantify the probability of having critical defects for stresses, in the whole loaded volume, below a threshold of interest.

6 | VHCF LIFE AND CRITICAL DEFECT SIZE DISTRIBUTIONS: PARAMETER ESTIMATION

The statistical distributions of the VHCF life and of the critical defect size (Equations 5 and 8, respectively) involve six parameters in total: c_Y, m_Y, n_Y, σ_Y, $\mu_{\sqrt{A}}$, and $\sigma_{\sqrt{A}}$. The parameters must be properly estimated with statistical estimation methods. Typically, when the statistical distributions are known, the maximum likelihood (ML) estimation principle is adopted for its good asymptotic properties.[60,61] The ML principle requires the maximization of the likelihood function, which depends on the parameters to be estimated and is computed from the

pdfs of Y and $\sqrt{A_c}$, f_Y, and $f_{\sqrt{A_c}}$. The pdfs of Y and $\sqrt{A_c}$ can be analytically defined from Equations 5 and 8 (i.e., $f_Y = \partial F_Y/\partial y$ and $f_{\sqrt{A_c}} = \partial F_{\sqrt{A_c}}/\partial\sqrt{a}$) and requires several numerical integrations to be computed. The numerical integrations must be replicated for each datapoint and must be iterated when maximizing the likelihood function. Each numerical integration is not immediate, and each iteration, run in Matlab with the Nelder–Mead maximization algorithm, can take up to 10 min. By considering at least 1000 iterations for getting the maximum value of the likelihood function, the estimated computational time for the parameter estimation would be larger than 150 h, which is not acceptable at all.

To reduce the computational time required for the parameter estimation, a different approach, based on Monte Carlo simulations, is applied in the following. The approach consists of the following steps:

1. Randomly generate, from a standard uniform distribution, $n_{sim} \times n_s \times n_{exp}$ samples (being n_{sim} larger than 1000, n_s equal to the number of uniformly stressed volumes and n_{exp} equal to the number of experimental failures). In the following, $u_{i,j,k}$ denotes, for the kth experimental failure occurred with maximum stress equal to $s_{max,k}$ (being $k = 1, ...,n_{exp}$), the ith random sample (with $i = 1,...,n_{sim}$) related to the jth uniformly stressed volume v_j (with $j = 1,...,n_s$).
2. Randomly generate, from a standard normal distribution, $n_{sim} \times n_s \times n_{exp}$ samples. In the following, $z_{i,j,k}$ denotes, for the kth maximum stress amplitude, the ith random sample related to the jth uniformly stressed volume v_j.
3. Define an initial guess for the six parameters $c_Y = c_Y^*$, $m_Y = m_Y^*$, $n_Y = n_Y^*$, $\sigma_Y = \sigma_Y^*$, $\mu_{\sqrt{A}} = \mu_{\sqrt{A}}^*$ and $\sigma_{\sqrt{A}} = \sigma_{\sqrt{A}}^*$.
4. Compute, from the truncated LEVD (Equation 1), n_{sim} random largest defect sizes, for each uniformly stressed volume v_j and for each maximum stress, as follows:

$$\begin{cases} \sqrt{a}_{i,j,k} = \mu_{\sqrt{A}_j} + \sigma_{\sqrt{A}}^* \left(-\log\left(-\log\left(p_{i,j,k}\right)\right)\right) \\ \mu_{\sqrt{A}_j} = \mu_{\sqrt{A}}^* + \sigma_{\sqrt{A}}^* \log\left(v_j\right) \\ p_{i,j} = e^{-e^{\mu_{\sqrt{A}_j}/\sigma_{\sqrt{A}}^*}} + u_{i,j,k}\left(1 - e^{-e^{\mu_{\sqrt{A}_j}/\sigma_{\sqrt{A}}^*}}\right) \end{cases}. \quad (13)$$

Equation 13 exploits the location-scale properties of the truncated LEVD distribution[62]; $\sqrt{a}_{i,j,k}$ denotes, for the kth maximum stress amplitude, the ith random sample related to the jth uniformly stressed volume v_j.

5. Compute, from the normal distribution (Equation 2), n_{sim} VHCF lives, for each uniformly stressed volume v_j and for each maximum stress amplitude, as follows:

$$\begin{cases} y_{i,j,k} = \mu_{Y_{i,j,k}} + \sigma_Y^* \cdot z_{i,j,k} \\ \mu_{Y_{i,j,k}} = c_Y^* + m_Y^* \log_{10}\left(s_{max,k}\left(\frac{s_j}{s_{max,k}}\right)\right) + n_Y^* \log_{10}\left(\sqrt{a}_{i,j,k}\right) \end{cases}. \quad (14)$$

Equation 14 exploits the location-scale properties of the normal distribution[62]; $y_{i,j,k}$ denotes, for the kth maximum stress amplitude, the ith random sample related to the jth uniformly stressed volume v_j.

6. Compute n_{sim} VHCF lives, for the whole loaded volume and for each maximum stress, as follows:

$$y_{failure,i,k} = y_{i,j^*,k} = \min\left[y_{i,1,k}, ..., y_{i,n_s,k}\right], \quad (15)$$

where j^* denotes the index corresponding to the minimum value among the random n_s VHCF lives extracted for each uniformly stressed volume; $y_{failure,i,k}$ denotes, for the kth maximum stress amplitude, the ith random VHCF life related to the whole loaded volume.

7. Compute n_{sim} critical defect sizes, for each maximum stress, as follows:

$$\sqrt{a}_{critical,i,k} = \sqrt{a}_{i,j^*,k}, \quad (16)$$

where $\sqrt{a}_{critical,i,k}$ denotes, for the kth maximum stress amplitude, the ith random critical defect size related to the whole loaded volume.

8. Gather together the $n_{sim} \times n_{exp}$ VHCF lives for the whole loaded volume and compute the simulated empirical cdf[62] for the VHCF failure.
9. Gather together the $n_{sim} \times n_{exp}$ critical defect sizes and compute the simulated empirical cdf for the critical defect size.
10. Compute the coefficient of determination R_Y^2 in a quantile–quantile (Q-Q) plot[63] comparing the experimental and the simulated quantiles of the VHCF failures.

11. Compute the coefficient of determination $R^2_{\sqrt{A}_c}$ in a Q-Q plot comparing the experimental and the simulated quantiles of the critical defect size.
12. Compute the total coefficient of determination $R^2_{tot} = R^2_Y + R^2_{\sqrt{A}_c}$.
13. Change the parameter values and repeat from step 3 until R^2_{tot} is maximum. The last set of parameter values, when R^2_{tot} reaches its maximum value, represents the set of estimates for the six parameters.

The proposed estimation procedure converges quite rapidly, and typically, less than 5 min are required for getting the estimates, provided that the initial guess is reasonable. A reasonable initial guess can be easily obtained by estimating the parameters of the statistical model that considers the 90% risk-volume. The reader may refer to Paolino et al.[52] for details about the procedure that must be followed to estimate the parameters of the model involving the 90% risk-volume.

7 | VHCF LIFE AND CRITICAL DEFECT SIZE: EXPERIMENTAL VALIDATION OF THE STATISTICAL MODELS

In this section, several experimental datasets are analyzed to validate the statistical models in Equations 5 and 8. The first two datasets are taken from experimental tests performed by the author and his coworkers and are detailed in previous studies.[25,26,42,44,52,64] The second two datasets are taken from the VHCF literature on size effect.[36] To evaluate the fitting performance of the proposed statistical models, experimental data are also analyzed with the traditional approach that considers the 90% risk-volume.[17,25,26,43–48,52] The cdf of the critical defect size, if the traditional approach is adopted, depends on two parameters, $\mu_{\sqrt{A},v_{90\%}}$ and $\sigma_{\sqrt{A},v_{90\%}}$, and is equal to

$$F_{\sqrt{A}_c,v_{90\%}}(\sqrt{a};v_{90\%}) = \frac{\phi_L\left(z_{\sqrt{A}_c,v_{90\%}}(\sqrt{a})\right) - \phi_L\left(z_{\sqrt{A}_c,v_{90\%}}(0)\right)}{1-\phi_L\left(z_{\sqrt{A}_c,v_{90\%}}(0)\right)}, \tag{17}$$

where $z_{\sqrt{A}_c,v_{90\%}}(\sqrt{a}) = \frac{\sqrt{a} - \left(\mu_{\sqrt{A},v_{90\%}} + \sigma_{\sqrt{A},v_{90\%}}\log(v_{90\%})\right)}{\sigma_{\sqrt{A},v_{90\%}}}$, $z_{\sqrt{A}_c,v_{90\%}}(0) = -\frac{\mu_{\sqrt{A},v_{90\%}} + \sigma_{\sqrt{A},v_{90\%}}\log(v_{90\%})}{\sigma_{\sqrt{A},v_{90\%}}}$, and $v^{90\%}$ denotes the 90% risk-volume. With the traditional approach, the cdf of the VHCF life depends on six parameters, $c_{Y,v_{90\%}}$, $m_{Y,v_{90\%}}$, $n_{Y,v_{90\%}}$, $\sigma_{Y,v_{90\%}}$, $\mu_{\sqrt{A},v_{90\%}}$, and $\sigma_{\sqrt{A},v_{90\%}}$, and is given by

$$F_{Y,v_{90\%}}(y;s_{max},v_{90\%}) = \int_0^\infty \phi_G\left(\frac{y-\mu_{Y,v_{90\%}}}{\sigma_{Y,v_{90\%}}}\right)\frac{1}{\sigma_{\sqrt{A},v_{90\%}}}\frac{\varphi_L\left(z_{\sqrt{A}_c,v_{90\%}}(\sqrt{a})\right)}{1-\phi_L\left(z_{\sqrt{A}_c,v_{90\%}}(0)\right)}d\sqrt{a}, \tag{18}$$

where $\mu_{Y,v_{90\%}} = c_{Y,v_{90\%}} + m_{Y,v_{90\%}}\log_{10}(s_{max}) + n_{Y,v_{90\%}}\log_{10}(\sqrt{a})$.

The comparison between the two approaches is carried out by computing the coefficients of determination, R^2_Y and $R^2_{\sqrt{A}_c}$, resulting from Q-Q plots of the estimated versus the experimental values. Q-Q plots are obtained from the estimated cdfs of the experimental VHCF lives and of the critical defect sizes, according to Benard's approximation for median ranks.[65] Equation 19 reports the cdf value for the ith sorted experimental failure:

$$F_{exp,i} = \frac{i-0.3}{N+0.4}, \tag{19}$$

where N is the total number of failures in the analyzed dataset.

The variation of the coefficients of determination with respect to the minimum stress ratio in the whole loaded volume (Figure 1) is also assessed. If the minimum stress ratio in the whole loaded volume is changed, then the number of uniformly stressed volumes changes as well: for a minimum stress ratio equal to 0%, then all the uniformly stressed volumes inside the whole loaded volume are considered, whereas for a minimum stress ratio equal to 90%, then the uniformly stressed volumes inside the 90% risk-volume are only considered. The analysis is performed with minimum stress ratios ranging from 0% to 90% with steps of 10%, to assess the capability of the proposed approach to identify statistical distributions whose parameters do not depend on the value of the minimum stress ratio.

7.1 | Tool steel: Gaussian versus hourglass

Fully reversed ultrasonic VHCF tests have been run in.[38,42,44,52,64,66] Tests have been performed on hourglass and Gaussian[37] specimens made of H13 steel. Twelve hourglass specimens with 90% risk-volume equal to 247 mm^3, and 18 Gaussian specimens with 90% risk-volume equal to 2278 mm^3 have been tested up to failure. Defects originating failures have been analyzed with the scanning electron microscope (SEM) and their size has

been measured following the square-root of area approach proposed by Murakami[17] and Matsunaga et al.[32] Further details on the experimental dataset are reported in previous works.[38,42,44,52,64,66]

The distribution of the uniformly stressed volume v with respect to the stress ratio s/s_{max} has been obtained with FEMs of the tested specimens. Modal analyses in Ansys software have been performed to get the stress distribution within the specimens during the ultrasonic test. Eight-node quadrilateral elements (plane 82) with the axisymmetric option are used for the FEMs. The average element size is 0.1 mm, ensuring mesh convergence. The material model considers a linear elastic isotropic steel (Young's modulus equal to 211,000 MPa, Poisson's ratio equal to 0.29, and material density equal to 7800 kg/m^3). Stress values are normalized with respect to the maximum value s_{max} within the volume. Then, the volumes with stress ratio larger than a specific minimum stress ratio ranging from 0% to 99.5% with steps of 0.5% have been computed: if the minimum stress ratio is equal to 0% then the whole volume is considered, whereas if it is equal to 99.5%, then the volume is quite smaller and has stress ratios ranging from 99.5% to 100%. The uniformly stressed volumes are finally computed as the differences between the adjacent volumes: for example, the first uniformly stressed volume, related to a stress ratio equal to 99.75%, corresponds to the volume with stresses ratios ranging from 99.5% to 100%; the second uniformly stressed volume, related to a stress ratio equal to 99.25%, is obtained by computing the difference between the volume with stress ratios ranging from 99% to 100% and the volume with stress ratios ranging from 99.5% to 100%; finally, the last uniformly stressed volume, related to a stress ratio equal to 0.25%, is obtained by computing the difference between the volume with stress ratios ranging from 0% to 100% and the volume with stress ratios ranging from 0.5% to 100%. To be more precise, the volumes are indeed quasi-uniformly stressed volumes, since the stress ratio is not constant in each volume but has a tolerance of ±0.25%. Figure 2 plots, for the two specimen shapes, the uniformly stressed volumes as a function of the stress ratio.

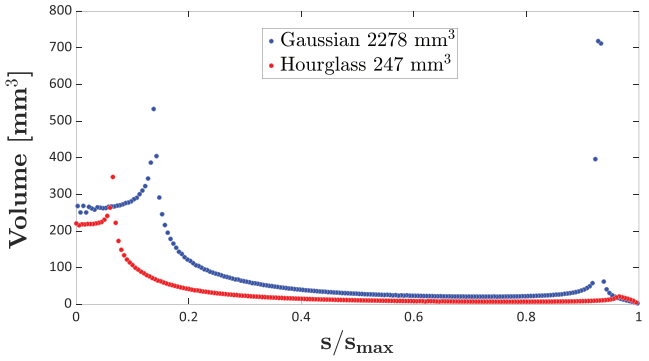

FIGURE 2 Distribution of uniformly stressed volumes in Gaussian and hourglass specimens[38,42,44,52,64,66] [Colour figure can be viewed at wileyonlinelibrary.com]

Parameters involved in the traditional approach with 90% risk-volume (Equations 17 and 18) are estimated with the ML principle, whereas parameters involved in the proposed approach (Equations 5 and 8) are estimated with the procedure described in Section 6. The estimates for the traditional approach are $c_{Y,v_{90\%}} = 65.03$, $m_{Y,v_{90\%}} = -18.85$, $n_{Y,v_{90\%}} = -2.422$, $\sigma_{Y,v_{90\%}} = 0.4118$, $\mu_{\sqrt{A},v_{90\%}} = -24.15$, and $\sigma_{\sqrt{A},v_{90\%}} = 7.656$, whereas the estimates for the proposed approach are $c_Y = 71.40$, $m_Y = -20.19$, $n_Y = -3.148$, $\sigma_Y = 1.113$, $\mu_{\sqrt{A}} = 8.565$, and $\sigma_{\sqrt{A}} = 5.547$. Figure 3A shows, for the two approaches, the variation of the coefficients of determination, R^2_Y and $R^2_{\sqrt{A_c}}$, resulting from Q-Q plots of the estimated versus the experimental values at different minimum stress ratios. The proposed approach (red and blue hollow circles in Figure 3A) outperforms the traditional approach (red and blue dots in Figure 3A). Furthermore, the R^2_Y and $R^2_{\sqrt{A_c}}$ computed with the proposed approach are constant (equal to 93% and 97%,

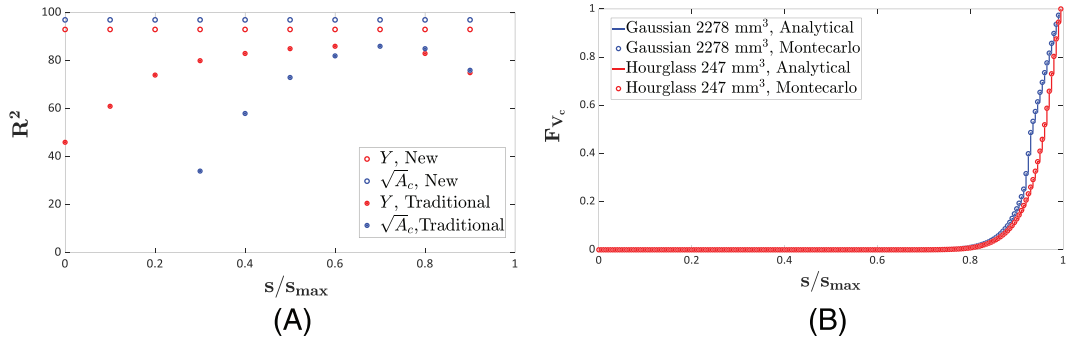

FIGURE 3 Effect of the minimum stress ratio for data in previous works[38,42,44,52,64,66]: (A) variation of the coefficients of determination; (B) cumulative distribution function of the critical volume [Colour figure can be viewed at wileyonlinelibrary.com]

respectively), regardless of the considered minimum stress ratio. Minimum stress ratios larger than 90% are not considered in the analysis, since they include an insufficient number of uniformly stressed volumes. This is confirmed by Figure 3B, which depicts the cdfs of the critical volume (Equation 12) for both specimen shapes. The probability of having critical volumes for minimum stress ratios larger than 90% is almost equal to 85%. Therefore, a nonnegligible quantity of critical volumes may be neglected (with probability larger than 15%) if the minimum stress ratio is set to values larger than 90%.

Hollow circles in Figure 3B also show the perfect agreement between the analytical approach (Equation 12) and the Monte Carlo approach (Section 6).

Figure 4 highlights the fitting capabilities of the proposed approach: Q-Q plots of the VHCF life (Figure 4A) and of the critical defect size (Figure 4C) show the agreement between the experimental data and the analytical models reported in Equation 5, for the VHCF life, and in Equation 8, for the critical defect size. The two Q-Q plots are obtained by considering a minimum stress ratio equal to 70% to be almost sure to include all the critical volumes in the analysis and, at the same time, to save computational time. Indeed, the plots and the coefficient of determination (Figure 3A) do not change for minimum stress ratios below 70% since the probability of having critical volumes for stress ratios below 70% is negligible. The good agreement shown in Figure 4A,C is also confirmed by the Anderson–Darling goodness of fit test,[63] whose p values are equal to 91.5% and 89.1% for the VHCF life and for the critical defect size, respectively.

Figure 4B,D shows the cdfs of the VHCF life (Equation 5) and of the critical defect size (Equation 8) for an applied stress equal to the mean value for each subset: for the Gaussian-specimen subset, the considered maximum stress is equal to 599 MPa, whereas for the hourglass-specimen subset, the considered maximum stress is equal to 635 MPa. For both subsets, Figure 4B,D highlights a good agreement with the experimental data. Figure 4C,D shows a larger number of datapoints (20 for the Gaussian-specimen subset and 18 for the hourglass-specimen subset) with respect to Figure 4A,B, since also runout specimens have been considered for the analysis.[38,42,44,52,64,66] It is worth to note that the mean stress well represents the whole subset, since the plotted datapoints are taken from all the applied stresses in each subset. Finally, hollow circles in Figure 4B,D again show the perfect agreement between the analytical approach (Equations 5 and 8) and the Monte Carlo approach (Section 6).

Figure 5 depicts the probabilistic-S-N (P-S-N) plot for the experimental data. The P-S-N curves corresponding to the αth quantiles, 10%, 50%, and 90%, are computed from Equation 5, by substituting F_Y with α and by solving

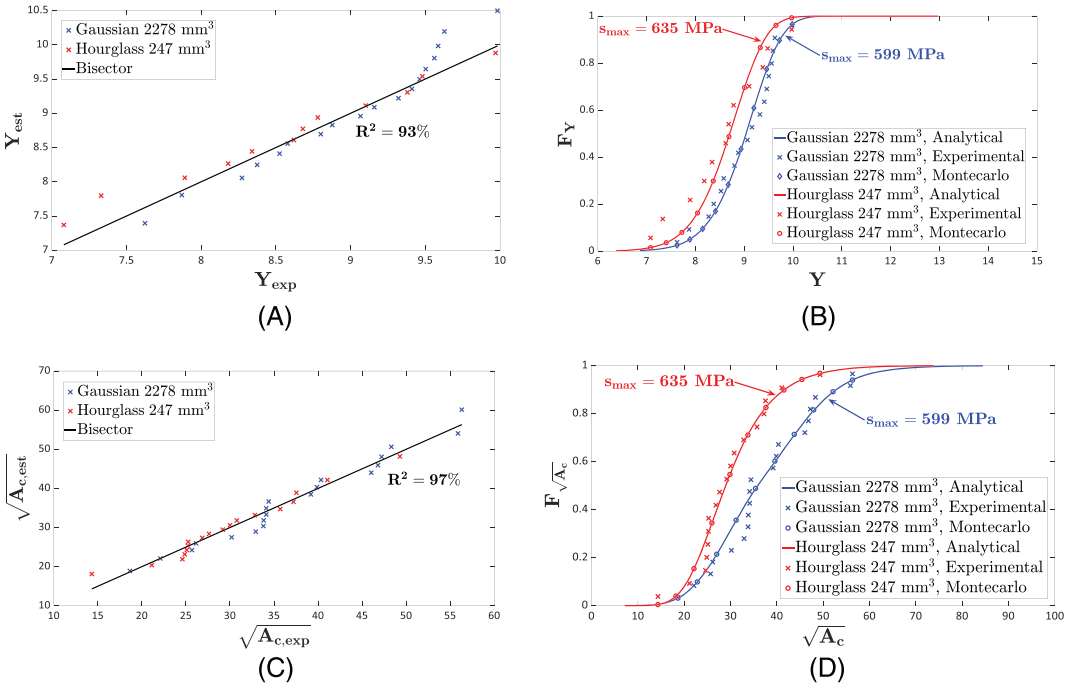

FIGURE 4 Fitting capabilities of the proposed approach for data in previous studies[38,42,44,52,64,66]: (A) Q-Q plot for the VHCF life; (B) dataset and cumulative distribution functions for the VHCF life; (C) Q-Q plot for the critical defect size; (D) dataset and cumulative distribution functions for the critical defect size [Colour figure can be viewed at wileyonlinelibrary.com]

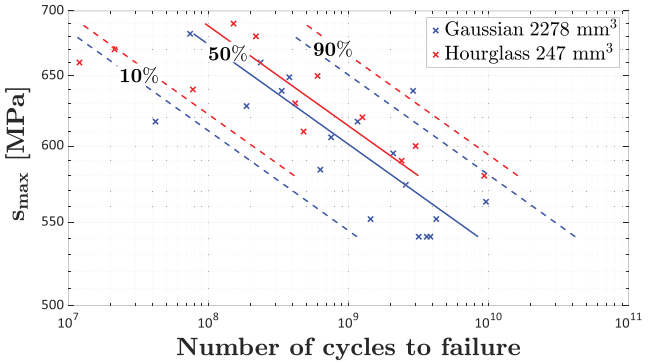

FIGURE 5 S-N plot of experimental data in previous works[38,42,44,52,64,66] and estimated P-S-N curves for Gaussian and hourglass specimens [Colour figure can be viewed at wileyonlinelibrary.com]

the Equation 5 with respect to y, for different values of s_{max}.

Size effects are clearly visible in Figure 5 as well as in Figure 4D: the larger Gaussian specimen exhibits smaller VHCF life and strength (blue curves in Figure 5) and larger critical defect size (blue curve in Figure 4D). It is worth to note that size effects are instead hindered in Figure 4B due to the partial overlap of the VHCF lives if all the applied maximum stresses are gathered together. Indeed, Figure 5 shows that, if the comparison is performed for each applied maximum stress, then the hourglass specimens exhibit, in average, larger VHCF lives with respect to the Gaussian specimens, thus highlighting size effects.

7.2 | Refined tool steel: Gaussian versus hourglass

Fully reversed ultrasonic VHCF tests have been run in previous studies.[39,42,44,66] Tests have been performed on hourglass and Gaussian specimens made of an H13 steel subjected to electro-slag-remelting (ESR) refinement process. Specimen geometries are the same analyzed in Section 7.1. Thirteen hourglass specimens with 90% risk-volume equal to 247 mm^3 and 16 Gaussian specimens with 90% risk-volume equal to 2278 mm^3 have been tested up to failure. Defects originating failures have been analyzed with the SEM and their size has been measured following the square root of area approach proposed by Murakami[17] and Matsunaga et al.[32] Further details on the experimental dataset are reported in previous works.[39,42,44,66]

The distribution of the uniformly stressed volume v with respect to the stress ratio s/s_{max} has already been reported in Section 7.1. Parameters involved in the traditional approach with 90% risk-volume and in the proposed approach are estimated with the procedure described in Section 7.1. The estimates for the traditional approach are $c_{Y,v_{90\%}} = 58.06$, $m_{Y,v_{90\%}} = -16.54$, $n_{Y,v_{90\%}} = -1.737$, $\sigma_{Y,v_{90\%}} = 0.6107$, $\mu_{\sqrt{A},v_{90\%}} = -4.472$, and $\sigma_{\sqrt{A},v_{90\%}} = 3.351$, whereas the estimates for the proposed approach are $c_Y = 44.42$, $m_Y = -9.059$, $n_Y = -5.278$, $\sigma_Y = 1.682$, $\mu_{\sqrt{A}} = 8.229$, and $\sigma_{\sqrt{A}} = 2.728$. Figure 6 shows, for the two approaches, the variation of the coefficients of determination, R^2_Y and $R^2_{\sqrt{A_c}}$, resulting from Q-Q plots at different minimum stress ratios. For minimum stress ratio smaller than 70%, the proposed approach (red and blue hollow circles in Figure 6) outperforms the traditional approach (red and blue dots in Figure 6).

For a minimum stress ratio equal to 90%, the proposed approach shows a drop in the coefficient of determination for the VHCF life, since an insufficient number of uniformly distributed volumes is considered if only stress ratios larger than 90% are taken into account. Indeed, the probability of having critical volumes for minimum stress ratios larger than 90% is equal to 52%, in case of Gaussian specimens, and to 54%, in case of hourglass specimens. Therefore, a nonnegligible quantity of critical volumes is neglected if the minimum stress ratio is set to values larger than or equal to 90%.

Figure 7 highlights the fitting capabilities of the proposed approach. The two Q-Q plots, obtained by considering a minimum stress ratio equal to 70%, show the agreement between the experimental VHCF lives (Figure 7A) and critical defect sizes (Figure 7B) and the analytical models in Equations 5 and 8. The good agreement shown in Figure 7A,B is also confirmed by the Anderson–Darling goodness of fit test,[63] whose p values are equal to 80.1% and 52.3% for the VHCF life and for the critical defect size, respectively. Figure 7B shows a larger number of datapoints (20 for the Gaussian-specimen subset and 16 for the hourglass-specimen subset) with respect to Figure 7A, since also

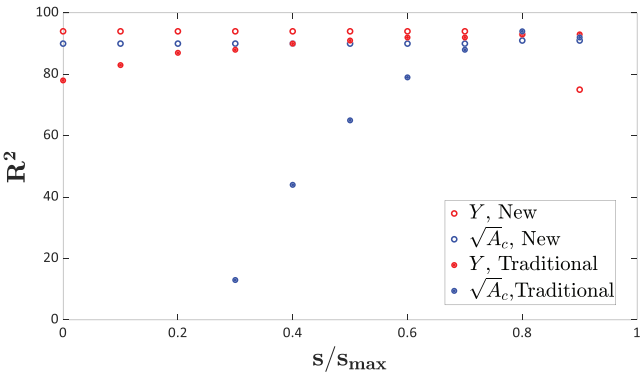

FIGURE 6 Variation of the coefficients of determination for different minimum stress ratios (experimental data reported in previous literature[39,42,44,66]) [Colour figure can be viewed at wileyonlinelibrary.com]

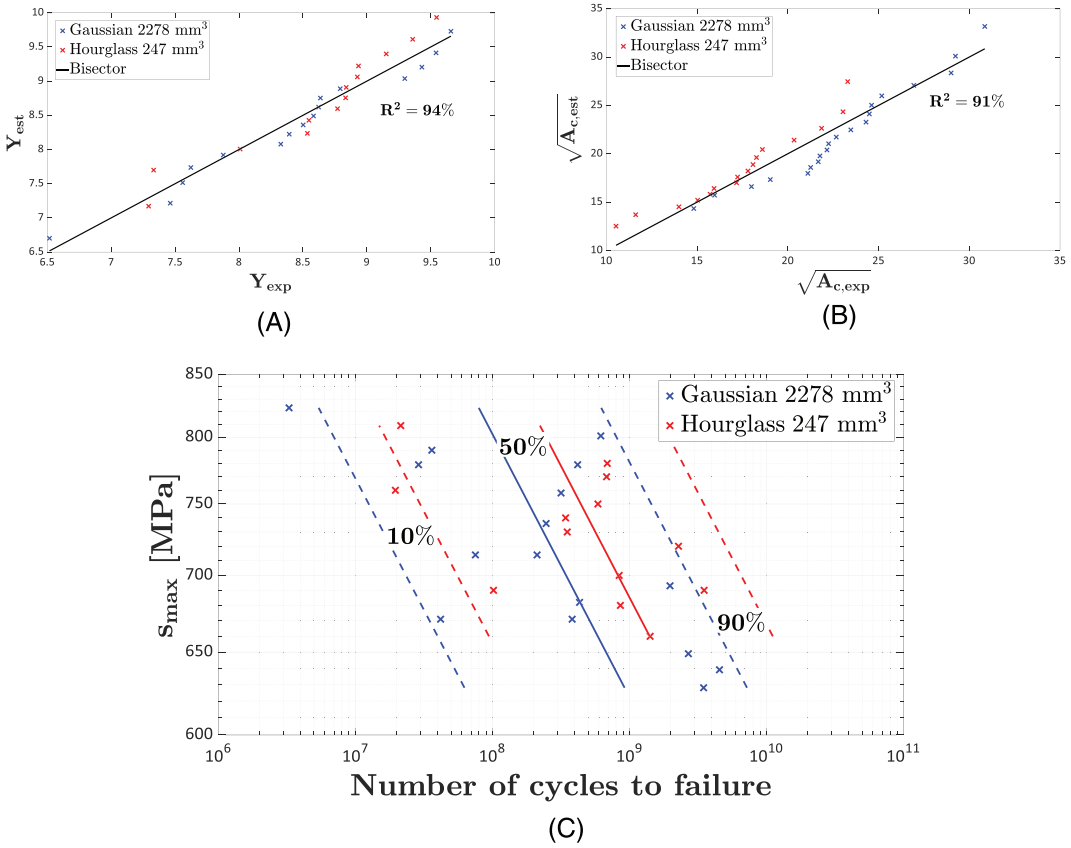

FIGURE 7 Fitting capabilities of the proposed approach for data in previous works[39,42,44,66]: (A) Q-Q plot for the VHCF life; (B) Q-Q plot for the critical defect size; (C) S-N plot of experimental data and estimated P-S-N curves for Gaussian and hourglass specimens [Colour figure can be viewed at wileyonlinelibrary.com]

runout specimens have been considered in the analysis.[39,42,44,66]

Figure 7C depicts the P-S-N plot for the experimental data. The P-S-N curves corresponding to the αth quantiles, 10%, 50%, and 90%, are computed following the procedure described in Section 7.1.

Size effects are clearly visible in Figure 7C: the larger Gaussian specimen exhibits smaller VHCF life and strength (blue curves in Figure 7C).

7.3 | Spring steel, heat B: Dog-bone versus hourglass

Fully reversed ultrasonic VHCF tests have been run in Furuya.[36] Tests have been performed on hourglass and dog-bone specimens made of a JIS-SUP7 spring steel subjected to two different heat treatments, called Heat B and Heat C. Further details on the heat treatments are provided in Furuya.[36] In this section, only specimens subjected to Heat B are analyzed. Thirteen hourglass specimens with 90% risk-volume equal to 29 mm^3 and eight dog-bone specimens with 90% risk-volume equal to 851 mm^3 have been tested up to failure. Defects originating failures have been analyzed with the SEM and their size has been measured following the square-root of area approach proposed by Murakami[17] and Matsunaga et al.[32] Further details on the experimental dataset are reported in Furuya.[36]

The distribution of the uniformly stressed volume v with respect to the stress ratio s/s_{max} is obtained with FEMs of the two specimen geometries, following the procedure reported in Section 7.1. Parameters involved in the traditional approach with 90% risk-volume and in the proposed approach are estimated with the procedure described in Section 7.1. The estimates for the traditional approach are $c_{Y,v_{90\%}} = 78.52$, $m_{Y,v_{90\%}} = -22.73$, $n_{Y,v_{90\%}} = -4.593$, $\sigma_{Y,v_{90\%}} = 0.3155$, $\mu_{\sqrt{A},v_{90\%}} = -5.151$, and $\sigma_{\sqrt{A},v_{90\%}} = 7.503$, whereas the estimates for the proposed approach are $c_Y = 85.77$, $m_Y = -23.55$, $n_Y = -7.517$, $\sigma_Y = 0.7459$, $\mu_{\sqrt{A}} = 3.381$, and $\sigma_{\sqrt{A}} = 6.788$. Figure 8A plots, for the two specimen shapes, the uniformly stressed volumes as a function of the stress ratio. Figure 8B shows, for the two approaches, the variation of the coefficients of determination, R^2_Y and $R^2_{\sqrt{A_c}}$, resulting from Q-Q plots at different minimum stress ratios. For all the investigated minimum stress ratios, the proposed approach (red and blue hollow circles in Figure 8B) is better or

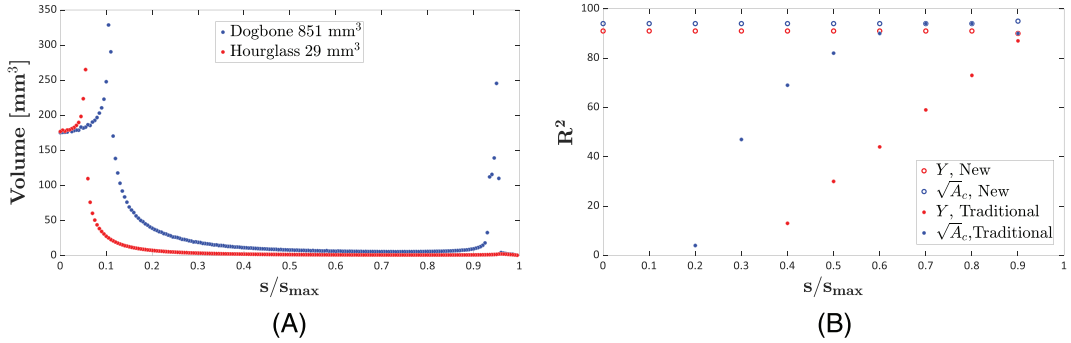

FIGURE 8 Effect of the minimum stress ratio for heat B specimens in Furuya[36]: (A) distribution of the uniformly stressed volume; (B) variation of the coefficients of determination [Colour figure can be viewed at wileyonlinelibrary.com]

equal than the traditional approach (red and blue dots in Figure 8B).

For a minimum stress ratio equal to 90%, the proposed approach shows small changes in the coefficients of determination, since an insufficient number of uniformly stressed volumes is considered if only stress ratios larger than 90% are taken into account. Indeed, the probability of having critical volumes for minimum stress ratios larger than 90% is equal to 80%, in case of dog-bone specimens. Therefore, a nonnegligible quantity of critical volumes is neglected if the minimum stress ratio is set to values larger than or equal to 90%.

Figure 9 highlights the fitting capabilities of the proposed approach. The two Q-Q plots, obtained by considering a minimum stress ratio equal to 70%, show the agreement between the experimental VHCF lives (Figure 9A) and critical defect sizes (Figure 9B) and the analytical models in Equations 5 and 8. The good

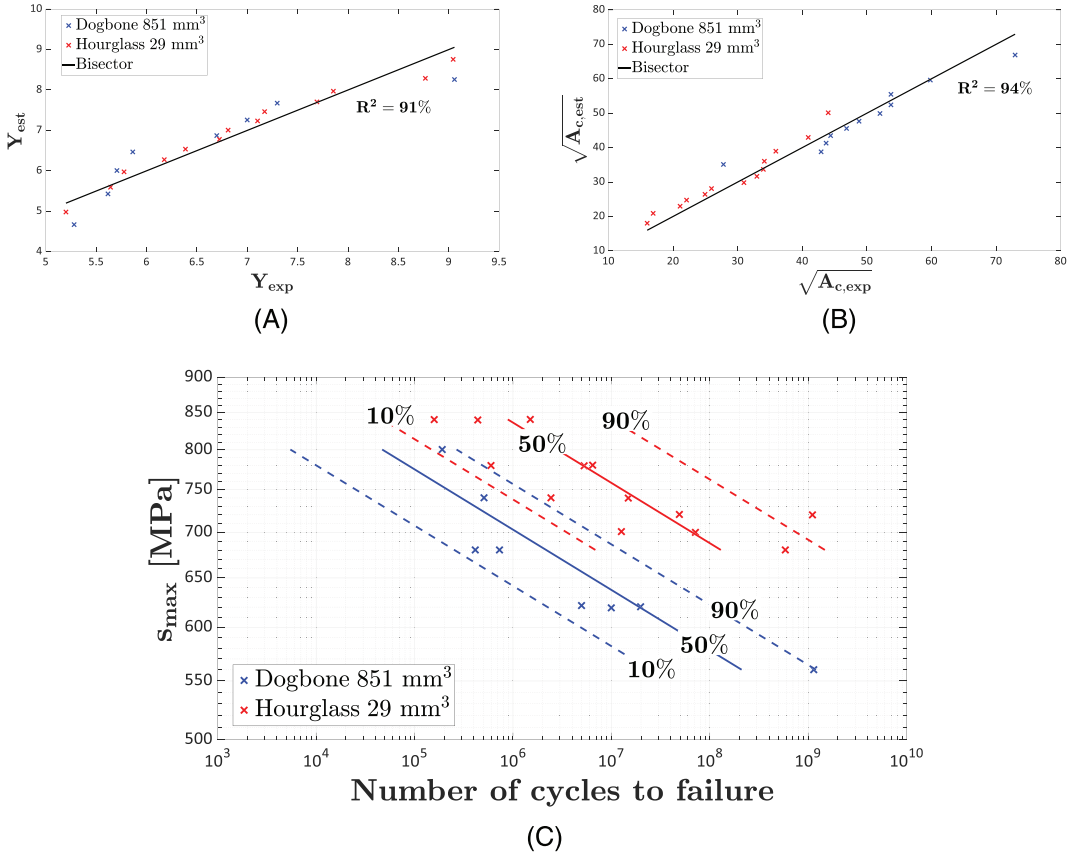

FIGURE 9 Fitting capabilities of the proposed approach for heat B specimens in Furuya[36]: (A) Q-Q plot for the VHCF life; (B) Q-Q plot for the critical defect size; (C) S-N plot of experimental data and estimated P-S-N curves for dog-bone and hourglass specimens [Colour figure can be viewed at wileyonlinelibrary.com]

agreement shown in Figure 9A,B is also confirmed by the Anderson–Darling goodness of fit test,[63] whose p values are equal to 71.0% and 82.8% for the VHCF life and for the critical defect size, respectively. Figure 9B shows a larger number of datapoints (11 for the dog-bone-specimen subset and 13 for the hourglass-specimen subset) with respect to Figure 9A, since also runout specimens have been considered for the analysis.[36]

Figure 9C depicts the P-S-N plot for the experimental data. The P-S-N curves corresponding to the αth quantiles, 10%, 50%, and 90%, are computed following the procedure described in Section 7.1.

Size effects are clearly visible in Figure 9C: the larger dog-bone specimen exhibits smaller VHCF life and strength (blue curves in Figure 9C).

7.4 | Spring steel, heat C: Dog-bone vs. hourglass

Fully reversed ultrasonic VHCF tests have been run in Furuya[36] on hourglass and dog-bone specimens made of a JIS-SUP7 spring steel subjected to two different heat treatments, called Heat B and Heat C. Further details on the heat treatments are provided in Furuya.[36] In this section, only specimens subjected to Heat C are analyzed. Eight hourglass specimens with 90% risk-volume equal to 29 mm^3 and nine dog-bone specimens with 90% risk-volume equal to 851 mm^3 have been tested up to failure. Defects originating failures have been analyzed with the SEM, and their size has been measured following the square root of area approach proposed by Murakami[17] and Matsunaga et al.[32] Only oxide-type inclusions have been considered in the analysis of the critical defect size, since these are the most critical defects originating failure in the investigated material.[36]

The distribution of the uniformly stressed volume v with respect to the stress ratio s/s_{max} is obtained with FEMs of the two specimen geometries, following the procedure reported in Section 7.1. Parameters involved in the traditional approach with 90% risk-volume and in the proposed approach are estimated with the procedure described in Section 7.1. The estimates for the traditional approach are $c_{Y,v_{90\%}} = 65.48$, $m_{Y,v_{90\%}} = -17.47$, $n_{Y,v_{90\%}} = -5.660$, $\sigma_{Y,v_{90\%}} = 0.7401$, $\mu_{\sqrt{A},v_{90\%}} = -5.1263$, and $\sigma_{\sqrt{A},v_{90\%}} = 4.5278$, whereas the estimates for the proposed approach are $c_Y = 78.43$, $m_Y = -22.62$, $n_Y = -2.887$, $\sigma_Y = 1.301$, $\mu_{\sqrt{A}} = -0.7009$, and $\sigma_{\sqrt{A}} = 6.631$. Figure 8A plots, for the two specimen shapes, the uniformly stressed volumes as a function of the stress ratio. Figure 10 shows, for the two approaches, the variation of the coefficients of determination, R^2_Y and $R^2_{\sqrt{A_c}}$, resulting from Q-Q plots at different minimum stress ratios. For minimum stress ratios smaller than 80%, the proposed approach (red and blue hollow circles in Figure 10) outperforms the traditional approach (red and blue dots in Figure 10).

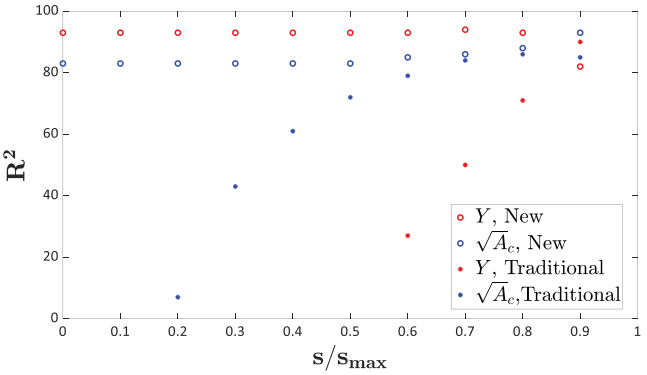

FIGURE 10 Variation of the coefficients of determination for different minimum stress ratios (experimental data for heat B specimens in Furuya[36]) [Colour figure can be viewed at wileyonlinelibrary.com]

For a minimum stress ratio equal to 90%, the proposed approach shows a drop in the coefficient of determination for the VHCF life, since an insufficient number of uniformly distributed volumes is considered if only stress ratios larger than 90% are taken into account. Indeed, the probability of having critical volumes for minimum stress ratios larger than 90% is equal to 67%, in case of dog-bone specimens, and to 47%, in case of hourglass specimens. Therefore, a non-negligible quantity of critical volumes is neglected if the minimum stress ratio is set to values larger than or equal to 90%.

Figure 11 highlights the fitting capabilities of the proposed approach. The two Q-Q plots, obtained by considering a minimum stress ratio equal to 70%, show the agreement between the experimental VHCF lives (Figure 11A) and critical defect sizes (Figure 11B) and the analytical models in Equations 5 and 8. The good agreement shown in Figure 11A.B is also confirmed by the Anderson–Darling goodness of fit test,[63] whose p values are equal to 79.4% and 55.4% for the VHCF life and for the critical defect size, respectively. Figure 11B shows a different number of datapoints (14 for the dog-bone-specimen subset and six for the hourglass-specimen subset) with respect to Figure 11A, since only oxide-type inclusions in runout and failed specimens have been considered for the analysis.[36]

Figure 11C depicts the P-S-N plot for the experimental data. The P-S-N curves corresponding to the αth quantiles, 10%, 50%, and 90%, are computed following the procedure described in Section 7.1.

Size effects are clearly visible in Figure 11C: the larger dog-bone specimen exhibits smaller VHCF life and strength (blue curves in Figure 11C).

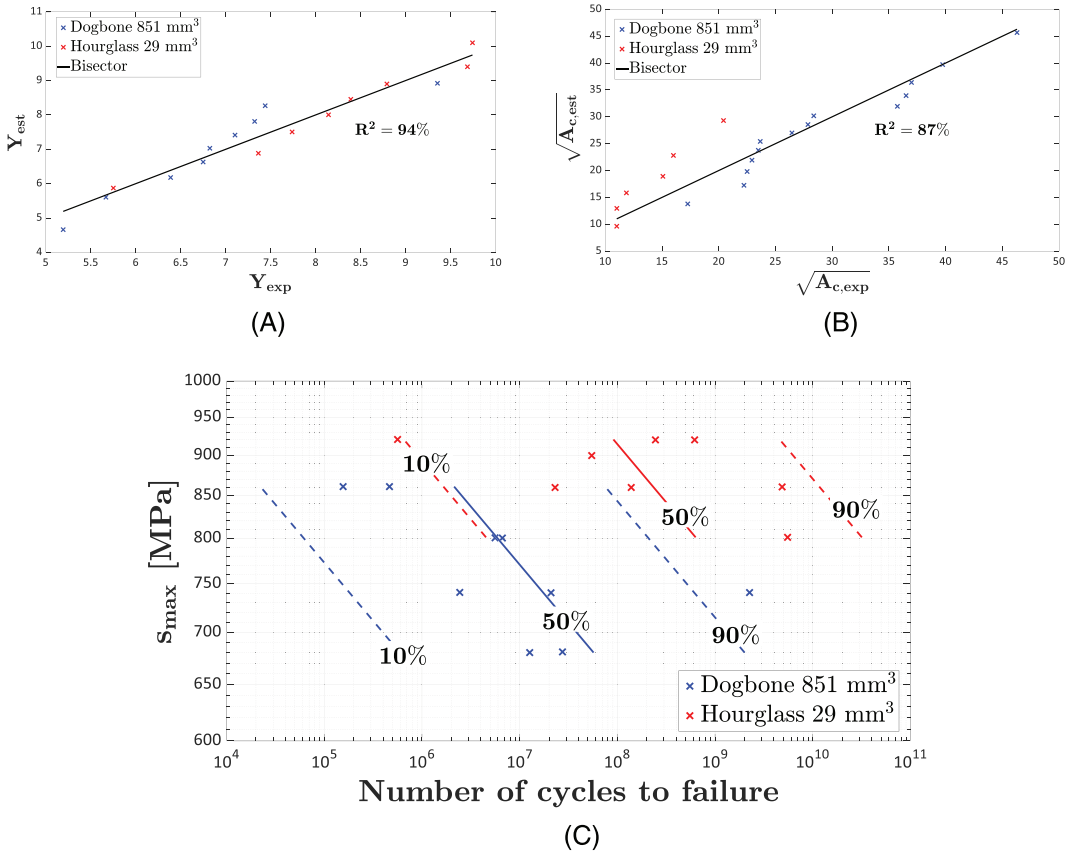

FIGURE 11 Fitting capabilities of the proposed approach for heat C specimens in Furuya[36]: (A) Q-Q plot for the VHCF life; (B) Q-Q plot for the critical defect size; (C) S-N plot of experimental data and estimated P-S-N curves for dog-bone and hourglass specimens [Colour figure can be viewed at wileyonlinelibrary.com]

8 | CONCLUSIONS

In the present paper, a novel statistical approach based on the weakest-link principle has been proposed to model size effects in VHCF. The statistical distributions of the VHCF life, of the size of the defect leading to VHCF failure (critical defect) and of the volume of material that contains the critical defect (critical volume) have been identified through direct application of the weakest-link principle and depend on six parameters that must be estimated from the experimental data. The identified statistical distributions are able to account for the stress distributions and the stress gradients that are present in a loaded material volume. The procedure for the parameter estimation is based on Monte Carlo simulations to reduce the computational time.

The main novelties of the present work can be thus summarized as follows:

- Novel quantitative evaluation of size effects in VHCF, based on the weakest-link principle.
- Original identification of the statistical distributions for the VHCF life, for the critical defect size, and for the critical volume.
- Proposal of an efficient and effective estimation method, based on Monte Carlo simulations, for estimating the parameters involved in the identified statistical distributions.

The theoretical results reported in the present paper can be usefully applied to predict the VHCF life of components, in-service conditions. The models can account for the actual large size of components[5–8,10] and for the actual geometry and loading conditions of components that may suffer from stress concentration, with stress gradients.

The proposed statistical models have been finally validated through experimental data taken from the literature and from VHCF tests run by the author and his coworkers. The experimental validation has proven the fitting capability of the proposed models. In particular, the following main conclusions can be drawn from the experimental validation:

- In terms of fitting capability, the proposed statistical models outperform the traditional models based on the 90% risk-volume.

- For a correct application of the proposed models, a sufficient number of uniformly stressed volumes must be considered in the analysis. For the investigated test cases, the minimum number of uniformly stressed volumes corresponds to the number of volumes with applied stress larger than 80% of the maximum applied stress. The smaller the percentage, the better. Though computationally expensive, the best analysis is the one that considers the whole loaded volume, that is, a percentage equal to 0%.
- The parameters involved in the proposed models can be considered as actual material parameters since they do not change if the whole loaded volume or a portion of it is considered in the analysis.
- The approach can account for notches. The stress gradients in notched regions originate a change in the distribution of the uniformly stressed volumes. This change causes, in turn, a change in the statistical distributions of the VHCF life and of the critical defect size.
- Differently from the traditional models based on the 90% risk-volume, with the proposed models there is no need of specifying a risk-volume.

The last conclusion is extremely relevant for designing machinery components against VHCF failure. Indeed, depending on the material, the percentage considered for computing the risk-volume could be inappropriate and, in particular, nonconservative. This risky occurrence is instead prevented if the models proposed in the present paper are applied.

DATA AVAILABILITY STATEMENT

Data sharing not applicable to this article as no datasets were generated or analyzed during the current study.

NOMENCLATURE

cdf	cumulative distribution function
c_Y , m_Y, n_Y	parameters involved in $\mu_{Y,i}$
$c_{Y,v_{90\%}}$, $m_{Y,v_{90\%}}$, $n_{Y,v_{90\%}}$, $\sigma_{Y,v_{90\%}}$, $\mu_{\sqrt{A},v_{90\%}}$, $\sigma_{\sqrt{A},v_{90\%}}$	parameters involved in $F_{Y,v_{90\%}}(\cdot)$
$f_{Y_i,\sqrt{A_i}\le\sqrt{a}}(\cdot)$	joint pdf of Y_i and $\sqrt{A_i}\le\sqrt{a}$
$f_{\sqrt{A_i}}(\cdot)$	pdf of $\sqrt{A_i}$
$F_{exp,i}$	empirical cdf for the ith experimental failure
$F_Y(\cdot)$	cdf of Y
$F_{Y_i}(\cdot)$	cdf of Y_i
$F_{Y_i\|\sqrt{a}}(\cdot)$	cdf of $Y_i\|\sqrt{a}$
$F_{Y,v_{90\%}}(\cdot)$	cdf of the VHCF life, 90% risk-volume approach
$F_{V_c}(\cdot)$	cdf of V_c
$F_{\sqrt{A_c}}(\cdot)$	cdf of $\sqrt{A_c}$
$F_{\sqrt{A_c},v_{90\%}}(\cdot)$	cdf of the critical defect size, 90% risk-volume approach
FEM	finite element model
LEVD	largest extreme value distribution
ML	maximum likelihood
N	total number of failures in the analyzed dataset
n_{exp}	number of experimental failures
n_s	total number of uniformly stressed volumes
n_{sim}	number of Montecarlo simulations
pdf	probability density function
P-S-N	probabilistic S-N
$p_{V_c}(\cdot)$	probability mass function of V_c
Q-Q	quantile–quantile
$R_{Y_i}(\cdot)$	reliability of Y_i, equal to $1-F_{Y_i}(\cdot)$
R^2_Y, $R^2_{\sqrt{A_c}}$, R^2_{tot}	coefficients of determination
rv	random variable
SEM	scanning electron microscope
s_i	ith local stress
s_{max} , $s_{max,k}$	maximum applied stress
VHCF	very high cycle fatigue
V_c	critical volume, rv
v_i	ith uniformly stressed volume
y , $y_{failure,i,k}$, $y_{i,j^*,k}$, $y_{i,j,k}$	VHCF life
Y	VHCF life, rv
Y_i	VHCF life related to v_i, rv
$Y_i\|\sqrt{a}$	conditional VHCF life related to v_i, rv
Y_{min}	minimum VHCF life among the uniformly stressed volumes
$\sqrt{A_c}$	critical defect size, rv
$\sqrt{A_i}$	largest defect size related to v_i, rv
$\sqrt{a}$, $\sqrt{a}_{i,j,k}$, $\sqrt{a}_{critical,i,k}$, $\sqrt{a}_{i,j^*,k}$	defect size
$\varphi_L(\cdot)$	pdf of the standardized LEVD
$\varphi_G(\cdot)$	pdf of the standardized normal distribution
$\phi_G(\cdot)$	cdf of the standardized normal distribution
$\phi_L(\cdot)$	cdf of the standardized LEVD
$\mu_{\sqrt{A}}$, $\sigma_{\sqrt{A}}$	parameters involved in the LEVD distribution
$\mu_{Y,i}$, σ_Y	parameters involved in $F_{Y_i\|\sqrt{a}}$
$\mu_{\sqrt{A},v_{90\%}}$, $\sigma_{\sqrt{A},v_{90\%}}$	parameters involved in $F_{\sqrt{A_c},v_{90\%}}(\cdot)$

ORCID

Davide S. Paolino https://orcid.org/0000-0002-4231-4580

REFERENCES

1. Bayraktar E, Garcias IM, Bathias C. Failure mechanisms of automotive metallic alloys in very high cycle fatigue range. *Int J Fatigue*. 2006;28(11):1590-1602.
2. Kumar A, Adharapurapu RR, Jones JW, Pollock TM. In situ damage assessment in a cast magnesium alloy during very high cycle fatigue. *Scripta Mater*. 2011;64(1):65-68.
3. Bathias C, Drouillac L, Le François P. How and why the fatigue S-N curve does not approach a horizontal asymptote. *Int J Fatigue*. 2001;23:143-151.
4. Marines I, Bin X, Bathias C. An understanding of very high cycle fatigue of metals. *Int J Fatigue*. 2003;25(9-11):1101-1107.
5. Esslinger V, Kieselbach R, Koller R, Weisse B. The railway accident of eschede—technical background. *Eng Fail Anal*. 2004;11(4):515-535.
6. Cong T, Han J, Hong Y, Domblesky JP, Liu X. Shattered rim and shelling of high-speed railway wheels in the very-high-cycle fatigue regime under rolling contact loading. *Eng Fail Anal*. 2019;97:556-567.
7. Klinger C, Bettge D. Axle fracture of an ICE3 high speed train. *Eng Fail Anal*. 2013;35:66-81.
8. Shanyavskiy AA. Fatigue limit—material property as an opened or closed system? Practical view on the aircraft components failures in GCF area. *Int J Fatigue*. 2006;28(11):1647-1657.
9. Bathias C, Paris PC. Gigacycle fatigue of metallic aircraft components. *Int J Fatigue*. 2010;32(6):894-897.
10. Shanyavskiy AA. Very-high-cycle-fatigue of in-service air-engine blades, compressor and turbine. *SCI CHINA Phys Mech Astron*. 2014;57(1):19-29.
11. Nikitin A, Bathias C, Palin-Luc T. A new piezoelectric fatigue testing machine in pure torsion for ultrasonic gigacycle fatigue tests: application to forged and extruded titanium alloys. *Fatigue Fract Eng Mater Struct*. 2015;38(11):1294-1304.
12. Nikitin A, Palin-Luc T, Shanyavskiy A, Bathias C. Comparison of crack paths in a forged and extruded aeronautical titanium alloy loaded in torsion in the gigacycle fatigue regime. *Eng Fract Mech*. 2016;167:259-272.
13. Naoe T, Xiong Z, Futakawa M. Gigacycle fatigue behaviour of austenitic stainless steels used for mercury target vessels. *J Nucl Mater*. 2016;468:331-338.
14. Zhang X, Liu X, Hong Y. Effects of specimen size on fatigue life of metallic materials in high-cycle and very-high-cycle fatigue regimes. *Fatigue Fract Eng Mater Struct*. 2016;39:770-779.
15. Jeddi D, Palin-Luc T. A review about the effects of structural and operational factors on the gigacycle fatigue of steels. *Fatigue Fract Eng Mater Struct*. 2018;41(5):969-990.
16. Bathias C, Paris PC. *Gigacycle Fatigue in Mechanical Practice*. CRC Dekker: USA; 2005.
17. Murakami Y. *Metal Fatigue: Effects of Small Defects and Nonmetallic Inclusions*. Elsevier Ltd: UK; 2002.
18. Borsato T, Ferro P, Berto F, Carollo C. Fatigue strength improvement of heavy-section pearlitic ductile iron castings by in-mould inoculation treatment. *Int J Fatigue*. 2017;102:221-227.
19. Borsato T, Ferro P, Berto F, Carollo C. Mechanical and fatigue properties of pearlitic ductile iron castings characterized by long solidification times. *Eng Fail Anal*. 2017;79:902-912.
20. Borsato T, Ferro P, Berto F, Carollo C. Influence of solidification defects on the fatigue behaviour of heavy-section silicon solution–strengthened ferritic ductile cast irons. *Fatigue Fract Eng Mater Struct*. 2018;41(11):2231-2238.
21. Borsato T, Ferro P, Berto F. Novel method for the fatigue strength assessment of heavy sections made by ductile cast iron in presence of solidification defects. *Fatigue Fract Eng Mater Struct*. 2018;41(8):1746-1757.
22. Borsato T, Ferro P, Berto F, Carollo C. Effect of solidification time on microstructural. Mechanical and Fatigue Properties of Solution Strengthened Ferritic Ductile Iron. *Metals*. 2019;9(24):1-12.
23. Bellini C, Di Cocco V, Favaro G, Iacoviello F, Sorrentino L. Ductile cast irons: microstructure influence on the fatigue initiation mechanisms. *Fatigue Fract Eng Mater Struct*. 2019;42(9):2172-2182.
24. Fernandino C, Tenaglia N, Di Cocco V, Boeri RE, Iacoviello F. Relation between microstructural heterogeneities and damage mechanisms of a ferritic spheroidal graphite cast iron during tensile loading. *Fatigue Fract Eng Mater Struct*. 2020;43(6):1262-1273.
25. Tridello A, Biffi CA, Fiocchi J, et al. VHCF response of as-built SLM AlSi10Mg specimens with large loaded volume. *Fatigue Fract Eng Mater Struct*. 2018;41(9):1918-1928.
26. Tridello A, Fiocchi J, Biffi CA, et al. Influence of the annealing and defects on the VHCF behavior of an SLM AlSi10Mg alloy. *Fatigue Fract Eng Mater Struct*. 2019;42(12):2794-2807.
27. Qian G, Li Y, Paolino DS, Tridello A, Berto F, Hong Y. Very-high-cycle fatigue behavior of Ti-6Al-4V manufactured by selective laser melting: effect of build orientation. *Int J Fatigue*. 2020;136(105628):1-13.
28. Qian G, Jian Z, Qian Y, Pan X, Ma X, Hong Y. Very-high-cycle fatigue behavior of AlSi10Mg manufactured by selective laser melting: effect of build orientation and mean stress. *Int J Fatigue*. 2020;138(105696):1-9.
29. Jian ZM, Qian GA, Paolino DS, Tridello A, Berto F, Hong YS. Crack initiation behavior and fatigue performance up to very-high-cycle regime of AlSi10Mg fabricated by selective laser melting with two powder sizes. *Int J Fatigue*. 2021;143(106013):1-12.
30. Du L, Qian G, Zheng L, Hong Y. Influence of processing parameters of selective laser melting on high-cycle and very-high-cycle fatigue behaviour of Ti-6Al-4V. *Fatigue Fract Eng Mater Struct*. 2021;44(1):240-256.
31. Murakami Y, Yokoyama NN, Nagata J. Mechanism of fatigue failure in ultralong life regime. *Fatigue Fract Eng Mater Struct*. 2002;25(8-9):735-746.
32. Matsunaga H, Sun C, Hong Y, Murakami Y. Dominant factors for very-high-cycle fatigue of high-strength steels and a new design method for components. *Fatigue Fract Eng Mater Struct*. 2015;38(11):1274-1284.
33. Beretta S, Anderson C, Murakami Y. Extreme value models for the assessment of steels containing multiple types of inclusion. *Acta Mater*. 2006;54(8):2277-2289.
34. Furuya Y. Specimen size effects on gigacycle fatigue properties of high-strength steel under ultrasonic fatigue testing. *Scripta Mater*. 2008;58(11):1014-1017.

35. Furuya Y. Size effects in gigacycle fatigue of high-strength steel under ultrasonic fatigue testing. *Procedia Eng*. 2010;2(1):485-490.
36. Furuya Y. Notable size effects on very high cycle fatigue properties of high-strength steel. *Mater Sci Eng a*. 2011;528(15):5234-5240.
37. Paolino DS, Tridello A, Chiandussi G, Rossetto M. On specimen design for size effect evaluation in ultrasonic gigacycle fatigue testing. *Fatigue Fract Eng Mater Struct*. 2014;37(5):570-579.
38. Tridello A, Paolino DS, Chiandussi G, Rossetto M. VHCF response of AISI H13 steel: assessment of size effects through Gaussian specimens. *Procedia Eng*. 2015;109:121-127.
39. Tridello A, Paolino DS, Chiandussi G, Rossetto M. VHCF strength decrement in large H13 steel specimens subjected to ESR process. *Procedia Struct Integrity*. 2016;2:1117-1124.
40. Paolino DS, Tridello A, Chiandussi G, Rossetto M. Crack growth from internal defects and related size-effect in VHCF. *Procedia Struct Integrity*. 2017;5:247-254.
41. Paolino DS, Tridello A, Chiandussi G, Rossetto M. Effect of defect size on P-S-N curves in very-high-cycle fatigue. *Procedia Struct Integrity*. 2017;7:335-342.
42. Tridello A, Paolino DS, Chiandussi G, Rossetto M. Effect of electroslag remelting on the VHCF response of an AISI H13 steel. *Fatigue Fract Eng Mater Struct*. 2017;40(11):1783-1794.
43. Tridello A, Fiocchi J, Biffi CA, et al. VHCF response of heat-treated SLM Ti6Al4V gaussian specimens with large loaded volume. *Procedia Struct Integrity*. 2019;18:314-321.
44. Tridello A. VHCF response of two AISI H13 steels: effect of manufacturing process and size-effect. *Metals*. 2019;9(133):1-11.
45. Tridello A, Paolino DS, Rossetto M. Ultrasonic VHCF tests on very large specimens with risk-volume up to 5000 mm^3. *Appl Sci*. 2020;10(2210):1–12.
46. Zhang JW, Lu LT, Wu PB, Ma JJ, Wang GG, Zhang WH. Inclusion size evaluation and fatigue strength analysis of 35CrMo alloy railway axle steel. *Mater Sci Eng a*. 2013;562:211-217.
47. Nie B, Chen D, Zhao Z, Zhang J, Meng Y, Gao G. Notch effect on the fatigue behavior of a TC21 titanium alloy in very high cycle regime. *Appl Sci*. 2018;8(1614):1-13.
48. Xue H, Sun Z, Zhang X, Gao T, Li Z. Very high cycle fatigue of a cast aluminum alloy: size effect and crack initiation. *J Mater Eng Perform*. 2018;27(10):5406-5416.
49. Fitzka M, Pennings B, Karr U, et al. Influence of cycling frequency and testing volume on the VHCF properties of 18Ni maraging steel. *Eng Fract Mech*. 2019;216(106525):1-9.
50. ASTM standard E2283-08. *Standard Practice for Extreme Value Analysis of Nonmetallic Inclusions in Steel and Other Microstructural Features*. ASTM International: USA; 2019.
51. Paolino DS, Tridello A, Chiandussi G, Rossetto M. Estimation of P-S-N curves in very-high-cycle fatigue: statistical procedure based on a general crack growth rate model. *Fatigue Fract Eng Mater Struct*. 2018;41(4):718-726.
52. Paolino DS, Tridello A, Chiandussi G, Rossetto M. S-N curves in the very-high-cycle fatigue regime: statistical modeling based on the hydrogen embrittlement consideration. *Fatigue Fract Eng Mater Struct*. 2016;39(11):1319-1336.
53. Pook LP. A 50-year retrospective review of three-dimensional effects at cracks and sharp notches. *Fatigue Fract Eng Mater Struct*. 2013;36(8):699-723.
54. Berto F, Pook LP, Campagnolo A. Corner point singularities under in-plane and out-of-plane loading: a review of recent results. *Eng Solid Mech*. 2017;5:167-176.
55. Sun C, Liu X, Hong Y. A two-parameter model to predict fatigue life of high-strength steels in a very high cycle fatigue regime. *Acta Mech Sin*. 2015;31(3):383-391.
56. Schuller R, Fitzka M, Irrasch D, Tran D, Pennings B, Mayer H. VHCF properties of nitrided 18Ni maraging steel thin sheets with different co and Ti content. *Fatigue Fract Eng Mater Struct*. 2015;38(5):518-527.
57. Li W, Yuan H, Wang P, Sakai T. Micro-defect effect on gigacycle fatigue S-N property and very slow crack growth of high strength low alloy steel. *Mater Sci Technol*. 2013;29(9):1101-1110.
58. Torabi AR, Campagnolo A, Berto F. Local strain energy density to predict mode II brittle fracture in Brazilian disk specimens weakened by V-notches with end holes. *Maternite*. 2015;69:22-29.
59. Berto F, Gallo P, Lazzarin P. High temperature fatigue tests of un-notched and notched specimens made of 40CrMoV13.9 steel. *Maternite*. 2014;63:609-619.
60. Bain LJ, Engelhardt M. *Statistical Analysis of Reliability and Life-Testing Models: Theory and Methods*. USA: Dekker; 1991.
61. Paolino DS, Cavatorta MP. Sigmoidal crack growth rate curve: statistical modelling and applications. *Fatigue Fract Eng Mater Struct*. 2013;36(4):316-326.
62. Stuart A, Ord JK, Arnold SF. *Kendall's Advanced Theory of Statistics: Classical Inference and the Linear Model*. . *Volume 2A*. USA: John Wiley; 2004.
63. D'Agostino RB, Stephens MA. *Goodness-of-fit-techniques*. UK: CRC press; 1986.
64. Tridello A, Paolino DS, Chiandussi G, Rossetto M. VHCF response of H13 steels produced with different manufacturing processes. *Procedia Eng*. 2016;160:93-100.
65. Benard A, Bos-Levenbach E-C. The plotting of observations on probability paper. *Statistica Neerlandica*. 1953;7(3):163-173.
66. Tridello A. VHCF response of Gaussian specimens made of high-strength steels: comparison between unrefined and refined AISI H13. *Fatigue Fract Eng Mater Struct*. 2017;40(10):1676-1689.

How to cite this article: Paolino DS. Very high cycle fatigue life and critical defect size: Modeling of statistical size effects. *Fatigue Fract Eng Mater Struct*. 2021;44:1209–1224. https://doi.org/10.1111/ffe.13424